A Novel Image Reconstruction Strategy for ECT: Combining Two Algorithms With a Graph Cut Method

Qiang Guo, Xue Li, Baolin Hou, Gregoire Mariethoz, Mao Ye, Wuqiang Yang, *Fellow, IEEE*, and Zhongmin Liu

***Abstract*— Image reconstruction plays a key role in the application of electrical capacitance tomography (ECT). Although many different algorithms have been developed in the past, it is often difficult to obtain satisfactory images in all imaging regions by the use of a single algorithm due to the soft-field nature of ECT. This motivated us to develop a novel ECT image reconstruction strategy, in which a high-quality image can be obtained by combining the images reconstructed by two different algorithms via a graph cut method. By doing so, it is possible to retain the advantage of each algorithm for specified imaging regions and improve the quality of the whole image. This strategy was verified both numerically and experimentally for two widely used ECT reconstruction algorithms, i.e., linear backprojection and Tikhonov regularization. The results for stationary objects as well as gas–solid fluidized beds demonstrated that this graph-cut-based combination strategy presents a promising approach for ECT image reconstruction.**

***Index Terms*— Electrical capacitance tomography (ECT), graph cut, image reconstruction algorithm, linear backprojection (LBP), Tikhonov regularization (TR).**

Manuscript received November 6, 2018; revised February 25, 2019; accepted February 27, 2019. This work was supported in part by the Newton Advanced Fellowship of the Royal Society, U.K., under Grant NA140308 and in part by the National Key Research and Development Program of China under Grant 2018YFB0604904. The Associate Editor coordinating the review process was Amitava Chatterjee. *(Corresponding authors: Xue Li; Mao Ye.)*

Q. Guo is with the Dalian National Laboratory for Clean Energy, Dalian Institute of Chemical Physics, Chinese Academy of Sciences, Dalian 116023, China, also with the National Engineering Laboratory for MTO, Dalian Institute of Chemical Physics, Chinese Academy of Sciences, Dalian 116023, China, and also with the University of Chinese Academy of Sciences, Beijing 100049, China (e-mail: guoqiang@dicp.ac.cn).

X. Li and B. Hou are with the State Key Laboratory of Catalysis, Dalian Institute of Chemical Physics, Chinese Academy of Sciences, Dalian 116023, China (e-mail: lixue@dicp.ac.cn; blhou@dicp.ac.cn).

G. Mariethoz is with the Institute of Earth Surface Dynamics, University of Lausanne, 1015 Lausanne, Switzerland (e-mail: gregoire.mariethoz@unil.ch).

M. Ye and Z. Liu are with the Dalian National Laboratory for Clean Energy, Dalian Institute of Chemical Physics, Chinese Academy of Sciences, Dalian 116023, China, and also with the National Engineering Laboratory for MTO, Dalian Institute of Chemical Physics, Chinese Academy of Sciences, Dalian 116023, China (e-mail: maoye@dicp.ac.cn; liuzm@dicp.ac.cn).

W. Yang is with the School of Electrical and Electronic Engineering, The University of Manchester, Manchester M13 9PL, U.K. (e-mail: wuqiang.yang@manchester.ac.uk).

Color versions of one or more of the figures in this paper are available online at http://ieeexplore.ieee.org.

Digital Object Identifier 10.1109/TIM.2019.2905282

I. Introduction

PROCESS tomography, since its inception in 1980s, has attracted considerable interest due to its ability to visualize and interpret complex two-phase flows in industrial processes [1], [2]. There are many different process tomography techniques due to different sensing schemes, such as X-ray tomography [3], Gamma-ray tomography [4], ultrasound tomography [5], electrical capacitance tomography (ECT), and microwave tomography [6]. Among them, ECT is the most mature one and has advantages of high temporal resolution, robustness, withstanding high temperature and high pressure, nonintrusiveness and noninvasiveness, and no radiation, which make it an ideal tool for measurement of highly dynamic two-phase flows encountered in many industries [7], [8]. So far, ECT has been successfully applied to the measurement of gas–solid fluidized beds [9]–[11], oil pipelines [12], combustion flame [13], and other industrial processes.

The principle of ECT is to reconstruct the permittivity distribution (and thus the material distribution) in the region of interest from the measured interelectrode capacitance via a specific image reconstruction algorithm. With the reconstructed image, some key parameters that are of industrial interests, for example, the bubble size in a gas–solid fluidized bed and oil fraction in an oil pipeline, can be obtained. Therefore, the image reconstruction algorithm plays a key role in the application of ECT [14]. However, two main difficulties are associated with the ECT image reconstruction. First, it is severely underdetermined due to that the number of capacitance measurements is far less than the number of pixels that need to be derived. Second, the ill-posed and ill-conditioned property of the sensitivity matrix makes the reconstructed images sensitive to measurement noise. To address these problems, many algorithms have been developed in the last two decades [9], [15]–[23], which include the simple linear backprojection (LBP) [22], Tikhonov regularization (TR) [21], Landweber iteration [20], and the deep learning method [16], just to name a few.

However, due to the soft-field nature of ECT, it is hard to obtain satisfactory images in all imaging regions by a single image reconstruction algorithm, and common knowledge is that some algorithms are good at reconstructing permittivity distribution in a specific region while some other algorithms

perform well in other regions. Considering this fact, an intuitive idea is to combine the images reconstructed by two different algorithms. Although the idea is straightforward, a simple image stacking method or weighted superposition cannot work satisfactorily in quantifying the gray values for each image pixel. Another avenue that directly combining two images to generate a new one by the use of the methods in computer graphics may offer an alternative way to overcome these difficulties. In this regard, the method of graph cut is considered in this paper. Graph cut has been widely used to construct digital images in the field of remote sensing [24], [25], medical science [26], and geophysics and geostatistical modeling [27], [28]. These works confirm the power of the graph cut method in image segmentation and synthesis. However, such a method has never been applied to tomographic image reconstruction. To this end, a novel ECT image reconstruction strategy is proposed in this paper, in which the ECT image quality can be improved via combining images reconstructed by two existing algorithms via the graph cut method.

To show the effectiveness of the proposed strategy, this paper focuses on two widely used algorithms for ECT, i.e., LBP and TR. These two algorithms are widely reported for on-line measurement due to their simplicity and fast speed. However, both algorithms show limitations in reconstructing ECT images. It has been found that images reconstructed by the LBP algorithm have no artifacts in the near-wall region but are blurred in the central region [9], [14], [29]. For the TR algorithm, conversely, although good results can be obtained in the central region, there are always artifacts in the near-wall region [9], [14], [23]. Therefore, these two algorithms are complementary and can be combined with the proposed strategy to improve the image quality. However, to the best of our knowledge, although substantial efforts have been devoted to improving the image quality reconstructed by these two algorithms, little work attempted to make the use of their complementarity and researchers usually tended to modify a certain algorithm. For example, Process Tomography Ltd. developed an iterative LBP algorithm [13]. Jing *et al.* [18] transformed the original image reconstruction problem to an optimization problem by adding an extended objective function to the TR algorithm. Xue *et al.* [23] reduced the artifacts by the TR algorithm by using a sensitivity matrix updated by the actual distribution. Inspired by the finding that the distribution of the artifacts is akin to the sensitivity distribution in the generic sensitivity matrix, Guo *et al.* [9] introduced a scaling method in the form of a division operation to the TR algorithm. Different from these studies, this paper demonstrates the possibility of improving the ECT image quality by combining two images reconstructed by these two algorithms.

The organization of this paper is as follows. First, the ECT imaging model and three widely used image reconstruction algorithms are briefly revisited. Then, the proposed graph-cut-based strategy is introduced. Next, the proposed strategy is verified both numerically and experimentally with the images reconstructed by the LBP and TR algorithms. This paper ends with some conclusions.

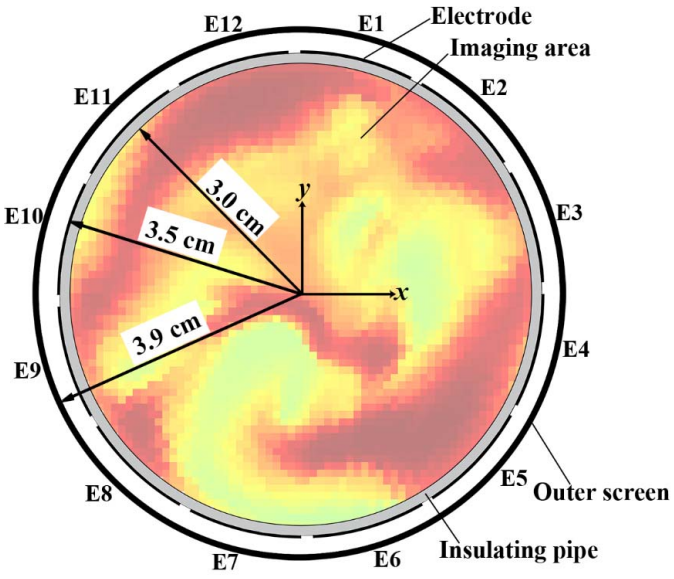

Fig. 1. Schematic of the simulated 12-electrode ECT sensor.

II. Fundamentals of ECT

A. ECT Imaging Model

Peng *et al.* [29] investigated the effect of the number of measurement electrodes on the image quality and suggested that 12-electrode sensors are suitable for most applications. Therefore, a circular 12-electrode sensor with the electrode covering ratio of 0.9 was modeled. Ye *et al.* [30] recently confirmed that such an electrode covering ratio can achieve good image quality. Fig. 1 shows the detailed dimensions of the modeled sensor. In a complete measurement procedure, one of the electrodes is selected, in turn, as the excitation electrode and others as detection electrodes to obtain the interelectrode capacitance between all possible electrode pairs. With this measurement strategy, the number of independent capacitance measurements is 66.

There are two computational problems encountered in ECT measurements, i.e., the forward problem and the inverse problem [9], [14].

The forward problem is to determine the interelectrode capacitance from a predefined sensor and permittivity distribution. The relationship between them is governed by

$$C_M = -\varepsilon_0 \frac{1}{V} \iint_{\Gamma} \varepsilon_r(x, y) \nabla \varphi(x, y) d\Gamma \tag{1}$$

where ε_0 is the permittivity of vacuum, V is the potential difference between two electrodes forming the capacitance, Γ is the electrode surface, and $\varepsilon_r(x, y)$ and $\varphi(x, y)$ are the relative permittivity and potential distributions in the sensing domain, respectively.

To simplify the calculation, a linear equation in a normalized form is usually used to replace (1)

$$\lambda = Sg \tag{2}$$

where g is the normalized permittivity and λ is the normalized capacitance. g and λ are defined, respectively, by

$$g = \frac{\varepsilon_r(x, y) - \varepsilon_L}{\varepsilon_H - \varepsilon_L} \tag{3}$$

$$\lambda = \frac{C_M - C_L}{C_H - C_L} \tag{4}$$

where ε_H and ε_L are, respectively, the relative permittivity of high- and low-permittivity materials to be imaged, C_M is the interelectrode capacitance for an arbitrary permittivity distribution, and C_H and C_L are the capacitances when the sensor is full of high- and low-permittivity materials, respectively.

In real measurement, the capacitance data are not noise-free. Therefore, (2) is changed to

$$\lambda = Sg + e \tag{5}$$

where e is the measurement noise. This equation can also be used to add white Gaussian noise to simulation data.

The parameter S in (2) and (5) is the normalized sensitivity matrix, representing the change in the normalized capacitance of each electrode pair in response to a perturbation in the normalized permittivity distribution. For implementation, the sensitivity matrix requires discretization. In this paper, a grid with 64×64 square elements is used, which results in 3228 effective pixels in the circular imaging area (see Fig. 1). Considering that there are 66 capacitance measurements for the 12-electrode ECT sensor, the dimensions of λ, S, and g in (1) are 66×1, 66×3228, and 3228×1, respectively.

The sensitivity matrix is usually calculated by numerical simulation of potential distribution in a vacuum based on the quasi-static field assumption and then by dot multiplying two potential distributions

$$S_{ij}^*(x, y) = -\iint_{p(x,y)} \frac{\nabla\varphi_i(x, y)}{V_i} \cdot \frac{\nabla\varphi_j(x, y)}{V_j} dxdy \tag{6}$$

where S_{ij}^* is the sensitivity between the ith and jth electrodes at the pixel $p(x, y)$, and $\varphi_i(x, y)$ and $\varphi_j(x, y)$ are the potential distributions when the ith and jth electrodes are excited by applying voltages of V_i and V_j, respectively.

Then, S^* is normalized as

$$S_{mn} = \frac{S_{mn}^*}{\sum_{n=1}^{N} S_{mn}^*} \tag{7}$$

where S_{mn} and S_{mn}^* are the elements in the mth row and nth column of S and S^*, respectively, and N is the number of pixels in the imaging area, which is 3228.

B. Image Reconstruction Algorithms

The inverse problem of ECT is to reconstruct the permittivity distribution from the measured interelectrode capacitance via a specific image reconstruction algorithm. In this section, three widely used algorithms, including LBP, TR, and Landweber iteration, are introduced, in which the former two are single-step, while the latter is iterative.

1) Linear Backprojection: LBP was the first developed algorithm for ECT [31]. Its principle is to replace the inverse of S, which does not exist, with the transpose of S, as formulated by

$$\hat{g} = \frac{S^T\lambda}{S^T u_\lambda} \tag{8}$$

where $\hat{g}$ is the reconstructed normalized permittivity in the image reconstructed by a certain algorithm and u_λ is a vector of ones with the same dimension as λ. Note that the division operation in (7) and (8) is manipulated in an elementwise mode, which means each numerator component is divided by the corresponding denominator component.

2) Tikhonov Regularization: TR, a well-established technique to solve ill-posed problems, has been extensively used in ECT image reconstruction [9], [18], [23]. Its formula is

$$\hat{g} = (S^T S + \mu I)^{-1} S^T \lambda \tag{9}$$

where μ is a regularization parameter and I is an $N \times N$ identity matrix. In general, a small value of μ is required to obtain a reliable approximation to the solution, which, however, may also lead to a singularity. For simplicity, in this paper, μ takes a constant value of 0.0001, as suggested by Guo *et al.* [9] via a trial and error study. In fact, there might be some alternative yet better methods, for example, the L-curve method [32] and generalized discrepancy principle [33] that can be used to obtain the optimal value of μ for a specified permittivity distribution.

3) Landweber Iteration: Landweber iteration is an iterative algorithm whose formula is written as

$$\hat{g}_k = P(\hat{g}_{k-1} + \alpha S^T(\lambda - S\hat{g}_{k-1})) \tag{10}$$

$$P[f(x)] = \begin{cases} 0, & \text{if } f(x) < 0 \\ f(x), & \text{if } 0 \le f(x) \le 1 \\ 1, & \text{if } f(x) > 1 \end{cases} \tag{11}$$

where α is the step length with the value of 2, k is the index of iteration steps, and P is a projection operator used to constrain the estimated image to ensure $\hat{g} \in [0, 1]$ [20]. The initial estimation $\hat{g}_0$ is calculated by the LBP algorithm as formulated in (8). A drawback of the Landweber algorithm rests with its semiconvergence, which means that the image quality is not always improved with the increase in the number of iterations. Usually, a predefined maximum iteration number is used and was set as 200 in this paper. Because the Landweber iteration algorithm has been confirmed to be capable of producing the best images in most cases [9], [14], it is used as a reference to assess the new proposed image reconstruction strategy.

III. Graph-Cut-Based Combination Strategy

In animation movies and video games, a large number of new images showing similar features as the sampled or training images are needed to display continuing movements or background landscapes. Image synthesis techniques are usually used to generate these new images by assembling irregular pieces of the sampled images and adjust them with seamless transitions [34]. From this point of view, the computer graphics technology has the potential to combine ECT images

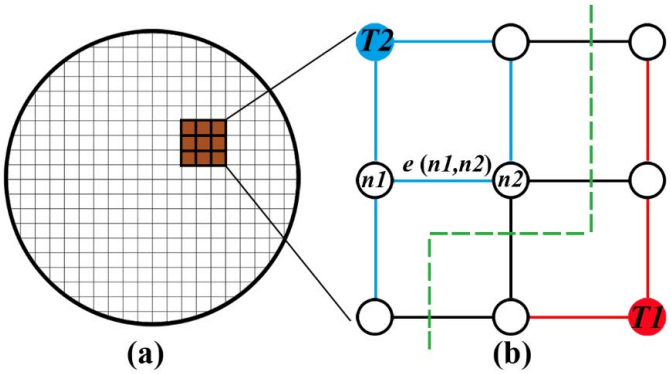

Fig. 2. Mapping an ECT-style image to a graph. (a) ECT-style image with 20×20 pixels. (b) Enlarged view of a graph that has the same configuration of (a) with n indicating the node and e indicating the edge connecting the neighbor nodes.

reconstructed by two algorithms. The synthesized image can keep good pieces of both images with the local artifacts in one image replaced by another image from the other algorithm.

To apply the computer graphics technology to ECT image reconstruction, the ECT-style image with pixel elements needs to be considered as a graph network. As an illustration, Fig. 2(a) shows an ECT-style image with 20×20 pixels, from where a subregion containing nine pixels is enlarged to represent the structure of a graph network, as shown in Fig. 2(b). Based on graph theory, each ECT pixel is mapped to a graph node n with the same geometrical configuration, and each node is connected to its nearest nodes by the relative edges e denoted as connecting lines in Fig. 2(b) [35]. A graph can be partitioned into two disjoint subsets that do not share any nodes and edges by a cut denoted as the green dashed line. As long as two images have an overlap, the overlap region can be considered as a graph and graph cut techniques can be used to analyze the similarity of the overlap and identify the optimal cut to seam these two images along the most similar passageway. In this sense, the graph cut problem is also known as a min-cut problem.

If two ECT images are reconstructed from the same measurement by two different algorithms A and B, the two images can be totally overlapped since they have the same geometry. To combine these two images, the absolute difference of the gray values (i.e., the reconstructed normalized permittivity) between them in each pixel is first calculated and assembled to an ECT-style image, which is then considered by graph cut methods as a graph, as shown in Fig. 2(b), with the graph nodes divided into two terminals (denoted as T1 and T2, respectively) and a set of nonterminal nodes (NT, denoted as hollow circles). The terminals T1 and T2 indicate, respectively, the nodes connected to the image reconstructed by Algorithms A and B. The values at each node are the absolute difference of the two ECT images. For example, the value of node $n1$ denoted as $\delta(n1)$ is calculated by

$$\delta(n1) = |\hat{g}_A(n1) - \hat{g}_B(n1)| \tag{12}$$

where $\hat{g}_A(n1)$ and $\hat{g}_B(n1)$ are the gray values from images reconstructed by Algorithms A and B, respectively. The capacity of the edges connecting $n1$ and $n2$, denoted as $e(n1, n2)$, is calculated by

$$e(n1,n2) = \delta(n1) + \delta(n2). \tag{13}$$

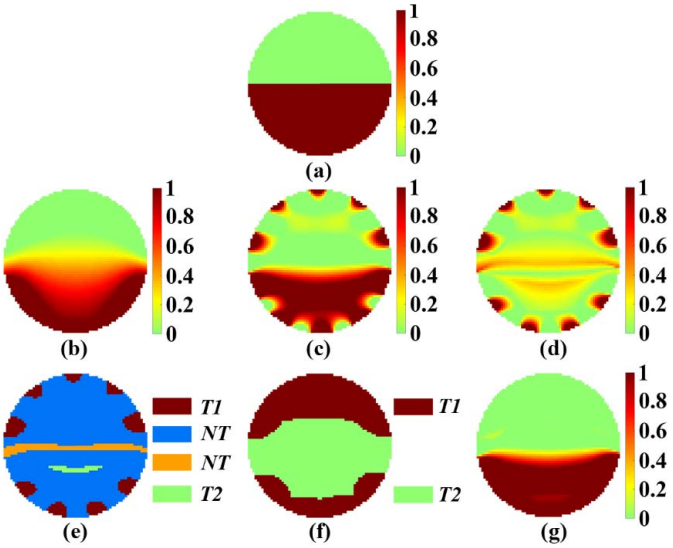

Fig. 3. Implementation of the graph cut method on images reconstructed by the LBP and TR algorithms. (a) True distribution. (b) Image reconstructed by the LBP algorithm. (c) Image reconstructed by the TR algorithm. (d) Absolute difference between (b) and (c). (e) Identification of the maximum different pieces and determination of the terminal and nonterminal nodes. (f) Labeling nodes with the graph cut method. (g) Final combined ECT image.

Once an edge is cut, the cut cost is assigned as the capacity of the edge. Therefore, the cut cost can be considered as the measurement of the similarity of the two images. Graph cut techniques, which are based on the min-cut theorem, find the cut that has the minimum total cost among all possible cuts throughout the graph, in order to separate NT into two sets: one set attached to T1 and the other attached to T2. According to this segmentation, the new image is constructed by assembling the pieces from the two images. Many algorithms have been developed for graph cut problems and the fast augmenting path algorithm proposed by Boykov and Kolmogorov [36] was used in this paper.

IV. Implementation on Images Reconstructed by the LBP and TR Algorithms

In the following, the proposed graph-cut-based strategy is implemented to combine two images reconstructed separately by the LBP and TR algorithms to show its capability to take advantages of both algorithms. Fig. 3 shows the process of the implementation of the graph-cut-based strategy for ECT image reconstruction. The true distribution is shown in Fig. 3(a). Fig. 3(b) and (c) shows the corresponding images reconstructed by the LBP and TR algorithms, respectively. It can be seen that the image reconstructed by the LBP algorithm has good quality in the near-wall region but poor accuracy in the central region, meanwhile the TR algorithm can perfectly present the central region but produce artifacts around the near-wall region. Note that the artifacts in the images reconstructed by the TR algorithm can be clearly identified, because the distribution of these artifacts shows certain common features. As can be seen in Fig. 3 and later in Figs. 5, 7, 9, 11,

and 12, for both stationary object distributions and two-phase flow patterns, the artifacts are formed with a high gray value displayed in pixels between two adjacent electrodes and low gray value in pixels near the electrode surface. As a result, the absolute difference of the two images reconstructed by the LBP and TR algorithms, as shown in Fig. 3(d), has several pieces with a relatively large value. A user-defined threshold, for example 0.85, i.e., the value above 85% nodes, is utilized to identify the large difference part. These identified pieces are divided into three kinds according to their locations, as shown in Fig. 3(e): 1) the pieces around the boundary (in red) are defined as terminal T1 and attached to the image reconstructed by the LBP algorithm; 2) the pieces in the center (in cyan) are defined as terminal T2 and attached to the image reconstructed by the TR algorithm; and 3) the pieces containing both the boundary and center nodes (in orange) are defined as the NT nodes. The background nodes (in blue) that have the difference value lower than the threshold are also defined as NT nodes. The graph-cut-based method labels the NT nodes as shown in Fig. 3(f) and seams the corresponding images together to form a new image, as shown in Fig. 3(g). As can be seen, the combined image visibly improves the image quality by taking advantages of the two algorithms.

Note that the user-defined threshold and the definition of terminals are the keys for the final results. The principle in determining the threshold is the identification of the most obvious difference in the absolute difference image. The optimal value of the threshold depends on the true distribution and the difference between the images used for combination. For the LBP and TR algorithms, the most obvious difference normally appears at the regions where the artifacts locate in the image reconstructed by the TR algorithm. Usually, a small value of the threshold will make the combined image like more that reconstructed by the TR algorithm, say the artifacts cannot be well removed, while a large value of the threshold will make the final image like more that by the LBP algorithm. Only the threshold within the range of 0.72–0.88 can remove all the artifacts in the near-wall region meanwhile retain the central region reconstructed by the TR algorithm, and when the threshold is in such range, the combined image quality does not change significantly with the change in the threshold. For convenience, a constant value of 0.85 was used in this paper. As will be seen in the following, such a value can give satisfactory results for all tested cases. In addition, using a constant value is necessary for on-line measurement, as determining the threshold needs additional computing time.

V. Evaluation Results and Discussion

Both numerical simulations with and without noise, as well as some experiments, were performed to evaluate the graph-cut-based strategy (GC_comb for short in the following text) based on the images reconstructed by the LBP and TR algorithms. Note that all numerical simulations were performed in 2-D.

The structure of the ECT sensor used in numerical simulations is detailed in Fig. 1. The simulation procedure is as follows. First, a specific permittivity distribution was defined in the imaging area. The low and high relative permittivity of the materials used was 1 and 3, respectively. Then, the forward problem was solved to obtain the inter-electrode capacitance. Finally, the obtained capacitance was converted to the reconstructed permittivity distribution using a specific image reconstruction algorithm. Such an arrangement allows to conveniently calculate the correlation coefficient (CC), which reflects the spatial similarity between the true and reconstructed distributions, to evaluate the performance of different image reconstruction methods quantitatively. The definition of CC is

$$\mathrm{CC} = \frac{\sum_{i=1}^{N} (\hat{g}_i - \bar{\hat{g}})(g_i - \bar{g})}{\sqrt{\sum_{i=1}^{N} (\hat{g}_i - \bar{\hat{g}})^2 \sum_{i=1}^{N} (g_i - \bar{g})^2}} \tag{14}$$

where $\bar{g}$ and $\bar{\hat{g}}$ are the mean values of g and $\hat{g}$, respectively. A larger CC usually indicates a better image quality [9], [14]. However, as the CC is a global quantity, sometimes, it may fail to reflect the local similarity between two images in certain cases. Therefore, it is better to consider both the reconstructed images and the associated CC in the comparison of different image reconstruction algorithms.

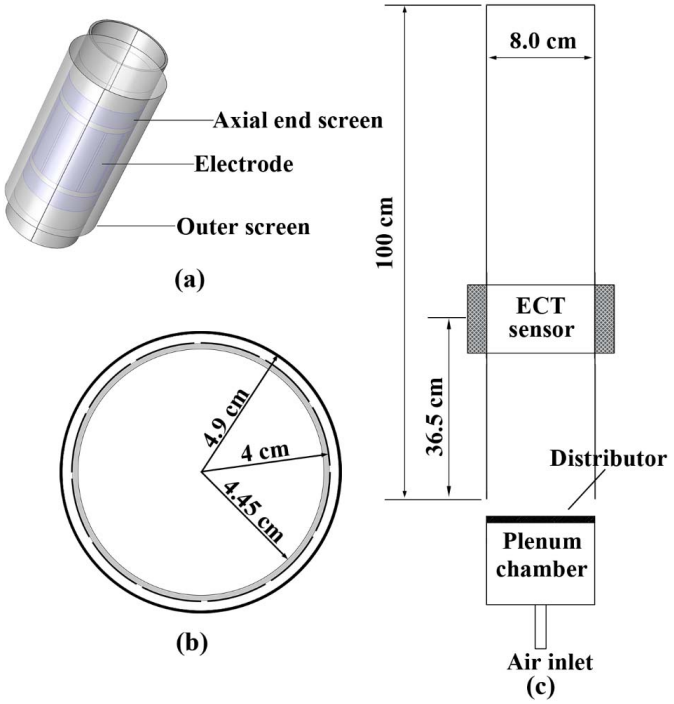

Fig. 4. Schematic of the ECT sensor used in experiments. (a) Axial view. (b) Cross-sectional view. (c) Installed on a fluidized bed.

Fig. 4(a) and (b) shows, respectively, the axial and cross-sectional view of the ECT sensor used in experiments; 12 measurement electrodes made of self-adhesive copper conducting sheet were stuck onto the outside wall of a quartz glass tube with the inner and outer diameter of 8 and 8.9 cm, respectively. The vertical height of the electrodes was 4 cm and the width was specified so that the electrode covering ratio keeps the same as that in simulations. Two axial end screens located at both axial ends of the measurement electrodes and an outer screen wrapped around the tube were connected to ground to eliminate external interference. The diameter of the outer

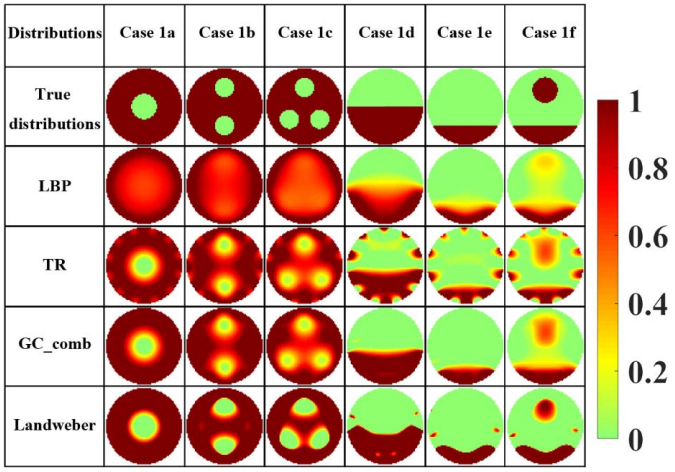

Fig. 5. Images reconstructed by different methods using simulation data with stationary object distributions.

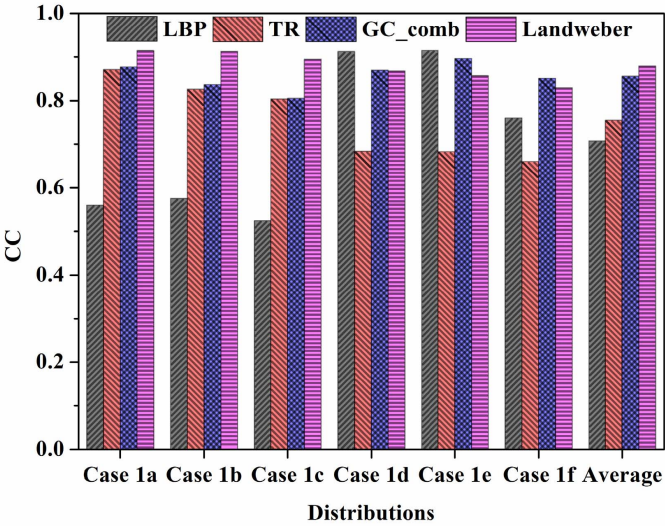

Fig. 6. CC of different methods using simulation data with stationary object distributions.

screen was 9.8 cm. An ac-based ECT system [37] was used for capacitance measurement. Besides some simple distributions with stationary objects, the sensor can also be installed on a fluidized bed, as shown in Fig. 4(c), to measure more complex distributions in a highly dynamic system. The gas and particles used in experiments were air and Al_2O_3 powder, which have the relative permittivity of 1 and 4, respectively. During calibration, the interelectrode capacitance was first measured as C_L when the bed was empty. Next, a known quantity of Al_2O_3 powder was poured into the bed and the bed was tapped to make the particles closely packed. The interelectrode capacitance at this state was measured as C_H. Such calibration endures that the interelectrode capacitance for all flow patterns lie within the range between C_L and C_H. Considering that the particle packing concentration at the closely packed state was about 0.63, the high relative permittivity used for calibration was 2.89 ($4 \times 0.63 + 1 \times 0.37 = 2.89$).

A. Evaluation by Numerical Simulations

Case 1: In Case 1, six simple permittivity distributions with the normalized permittivity of 0 and 1, as shown in Fig. 5, were used as the true distributions to evaluate the image quality reconstructed by different methods, in which cases 1a–1c represent bubble flows, cases 1d and 1e represent stratified flows, and case 1f represents bubble-stratified flow. The quantitative comparison of CC for different methods is plotted in Fig. 6. As can be seen, for the three bubble flows, the images reconstructed by the LBP algorithm are blurred in the central region and CC is also the lowest among all methods, which make it hard to identify the number of bubbles in the imaging area. While for the TR algorithm, although artifacts are shown in the near-wall region, the bubbles in the central region can be well captured. For the two stratified flows in cases 1d and 1e, the LBP algorithm has the highest CC, which is in agreement with the conclusion by Peng *et al.* [29] that the LBP algorithm can provide good images for stratified distributions. Even so, it is noted that the boundary between the high- and low-permittivity materials by the LBP algorithm is indistinct. In addition, when a bubble also appears in the stratified flow (case 1f), the CC decreases significantly. In contrast, when the TR algorithm is used, a clear boundary can be identified and the bubble in the stratified flow as shown in case 1f can also be identified. But still, the artifacts in the near-wall region worsen the overall image quality, as indicated by the lowest CC for cases 1d–1f in Fig. 6. The GC_comb method proposed in this paper can combine the advantages of both the LBP and TR algorithms and meanwhile abandon their disadvantages. Therefore, images reconstructed by the GC_comb method are all satisfied, as shown in Fig. 5, that the artifacts in the near-wall region are all well removed and good image quality in the central region reconstructed by the TR algorithm is retained. Fig. 6 also shows the average CC for all tested distributions with different methods. Clearly, the average CC obtained by the GC_comb method is higher than that obtained by both the LBP and TR algorithms, indicating that the GC_comb method can be applied in a more general and robust sense. A direct comparison of the reconstructed image quality between the GC_comb and Landweber iteration methods, as shown in Fig. 5, indicates that the images reconstructed by the GC_comb are similar to those by the Landweber iteration method with respect to the number and shape of the objects in the imaging area. In cases with stratified distributions shown in cases 1d–1f, the results by the GC_comb are even better, because some artifacts are also shown in the images reconstructed by the Landweber iteration method.

Case 2: To evaluate the performance of different image reconstruction algorithms, it is a common practice to perform numerical simulations and/or experiments with stationary objects [38]. In this way, only some simple distributions with binary models like those shown in Fig. 5 can be tested. However, real distributions in two-phase flows are much more complex due to the so-called chaotic behavior [39]. Therefore, it is necessary to introduce the two-phase flow characteristics to the evaluation of an image reconstruction algorithm. Recently, Guo *et al.* [9] reported such a framework based on computational fluid dynamic (CFD) and electrostatic

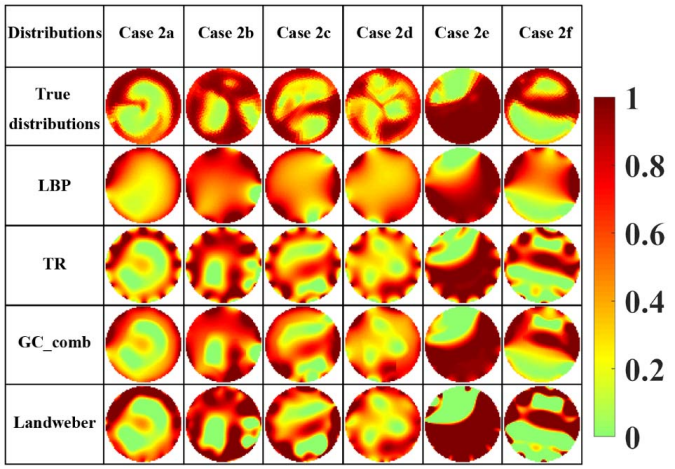

Fig. 7. Images reconstructed by different methods using CFD simulation results as the input permittivity distributions.

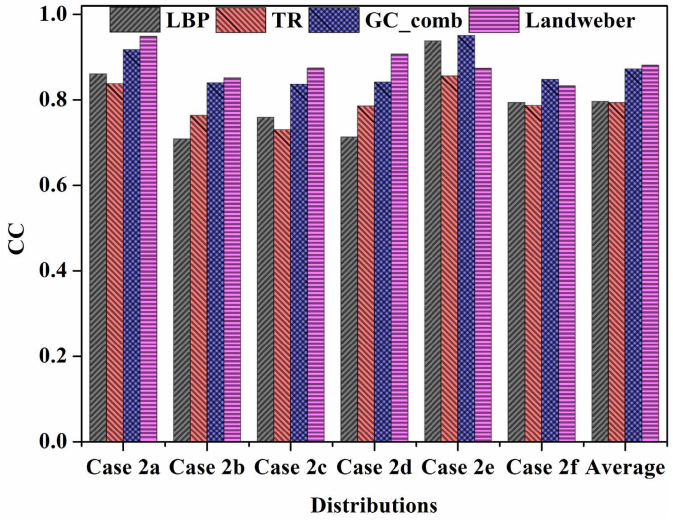

Fig. 8. CC of different methods using CFD simulation results as the input permittivity distributions.

simulations. First, 3-D CFD simulation of the investigated two-phase flow system, for example, a gas–solid fluidized bed, is performed. Then, some 2-D phantoms are extracted from the specified slices, i.e., the cross-sectional planes, of 3-D CFD simulation results. Next, these collected phantoms are used as the input permittivity distributions for ECT numerical simulations. Upon solving the forward problem, the interelectrode capacitance for a specified phantom can be obtained, which can be further used to reconstruct an image by a specific image reconstruction algorithm. By this way, the reconstructed images can be directly compared to the material distributions extracted from CFD simulation results that are akin to the true distributions in a two-phase flow system.

Fig. 7 shows six permittivity distributions obtained following the framework of Guo *et al.* [9] for a gas–solid fluidized bed, alongside the reconstructed images by different image reconstruction methods. The corresponding quantitative comparison regarding CC is shown in Fig. 8. Within the six distributions, case 2a represents the appearance of single bubble, cases 2b–2d represent multiple bubbles, case 2e represents

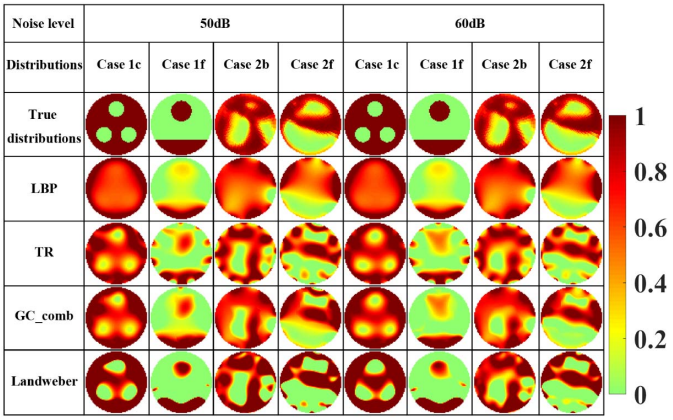

Fig. 9. Images reconstructed by different methods using simulation data with noise.

stratified distribution, and case 2f represents bubble-stratified distribution. As can be seen, similar to the analysis in Case 1, the GC_comb method can retain the good image quality reconstructed by the TR algorithm in the central region and, at the same time, avoid the appearance of artifacts in the near-wall region by the combination with the LBP algorithm. Therefore, satisfactory results can be obtained by the GC_comb method. More specifically, in cases 2a–2d for the single- and multiple-bubble distributions, the images reconstructed by the GC_comb method are very similar to those by the Landweber iteration algorithm. In cases with stratified distributions shown in cases 2e and 2f, the results by the GC_comb method are even better.

Case 3: Image reconstruction with ECT is a typical ill-posed problem, whose results are sensitive to measurement noise. The typical signal-to-noise ratio (SNR) of an ECT system is usually higher than 50 dB [40], [41]. Therefore, to evaluate the noise immunity of the proposed method, 50- and 60-dB white Gaussian noise was added to the interelectrode capacitance for the distributions shown in Cases 1 and 2. Fig. 9 shows some examples reconstructed by different image reconstruction methods using the data with noise. The average CC for all the 12 distributions in Cases 1 and 2 is shown in Fig. 10.

As can be seen, the added noise has no significant effect on the image quality obtained by the LBP algorithm for all distributions, which is consistent with the previous study [38]. While for other methods, with the increase in the noise level, the image quality gets worse. Nevertheless, the GC_comb method is always superior to the LBP and TR algorithms, indicating that the GC_comb method can be effectively used in noisy environments. Especially, the GC_comb method even performs better than the Landweber iteration method when 50-dB noise is added. This is because the noise may be propagated during the process of iteration when a relatively large noise is added for the Landweber iteration method [38].

B. Evaluation by Experiments

Case 4: To validate the simulation results and further verify the feasibility as well as the noise immunity of the proposed

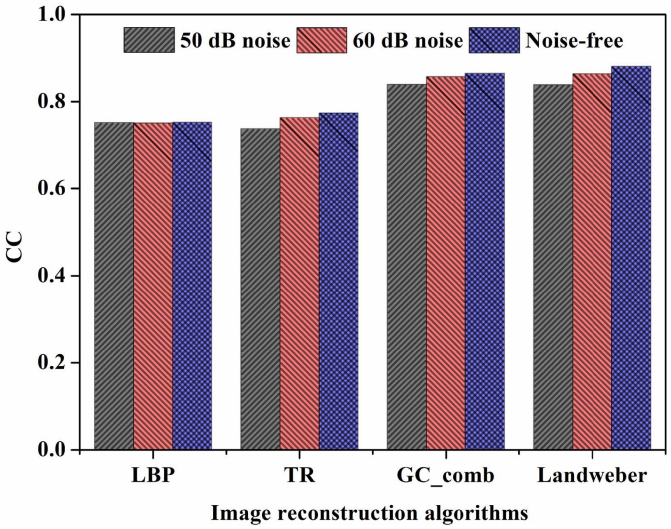

Fig. 10. CC of different methods using simulation data with noise.

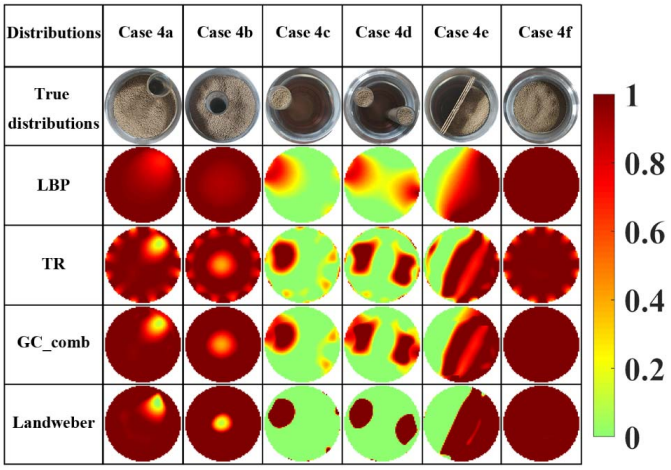

Fig. 11. Images reconstructed by different methods using experimental data with stationary object distributions.

GC_comb method, experiments with both stationary objects and a real gas–solid fluidized bed were performed. In this case, the reconstructed images with stationary object distributions by different methods are shown, as seen in Fig. 11, in which cases 4a and 4b were made by inserting an empty glass tube in the packed bed; cases 4c and 4d were made by inserting one and two glass tubes full of Al_2O_3 powder, respectively, to the empty bed; cases 4e and 4f represent a half-packed bed separated by a pasteboard and a fully packed bed, respectively. The outer diameter of the glass tube used was 2 cm for cases 4a–4c, while 1.5 cm for case 4d. The height of the targets used to produce these distributions was higher than that of the ECT sensor. The positions of the targets were not precisely oriented, while their approximate positions can be clearly seen in Fig. 11. The SNR of the used ECT system was about 58 dB, which is between the two SNR levels used in numerical simulations. It can be seen in Fig. 11 that the images reconstructed using the LBP and TR algorithms show similar features to those in numerical simulations, say the images by the LBP algorithm are blurred in the central region and the images by the TR algorithm show many artifacts in the

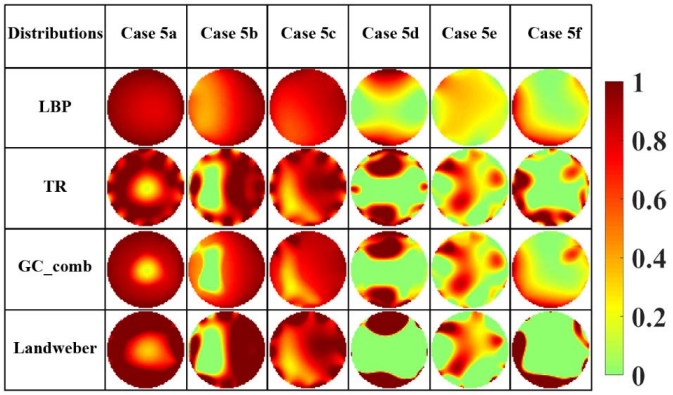

Fig. 12. Images reconstructed by different methods using experimental data from a gas–solid fluidized bed.

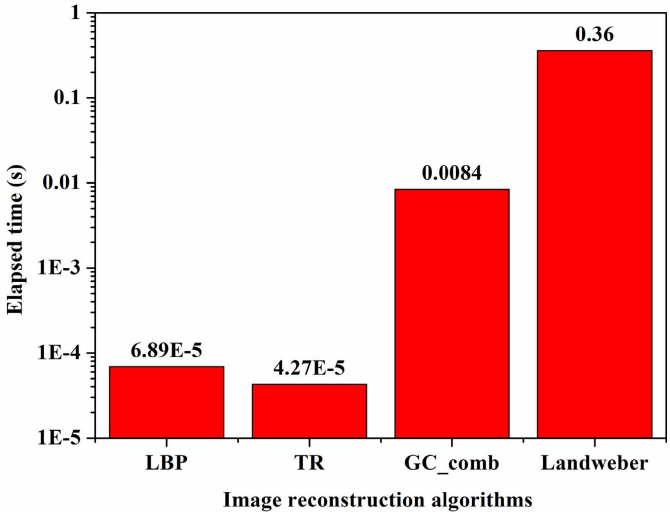

Fig. 13. Computational cost of different methods in a reconstruction step.

near-wall region. After combining these two images by the use of the GC_comb method, the drawbacks of both the LBP and TR algorithms are removed. Finally, satisfactory image quality, which is similar to that by the Landweber iteration algorithm, can be obtained by the GC_comb method with respect to the number and shape of the objects in the imaging area.

Case 5: In this case, the reconstructed images from a real gas–solid fluidized bed by different methods are shown, as seen in Fig. 12. Although true distributions are unknown, it is still clear in Fig. 12 that the GC_comb method can extract the distribution reconstructed by the TR algorithm in the central region and the distribution reconstructed by the LBP algorithm in the near-wall region to form a new image, which finally results in images as good as those by the Landweber iteration algorithm. Such results further confirm the feasibility of the graph-cut-based strategy in reconstructing material distributions in gas–solid two-phase flows.

C. Computational Cost Comparison

One of the most attractive advantages of ECT is its high temporal resolution. The typical measuring speed of commercial ECT systems is about 100 frames/s [8]. Therefore, an image reconstruction algorithm that can reconstruct images

at a speed faster than 100 frames/s is necessary to make full use of the commercial ECT systems and achieve the goal of on-line measurement. Fig. 13 compares the elapsed time in a reconstruction step required for different methods on a PC with an Intel Core i5 3.30 GHz. Note that the data in Fig. 13 were averaged over all the tested distributions shown before and each distribution was reconstructed 10 000 times. As can be seen, as only one step is involved, the LBP and TR algorithms are very fast with a reconstruction time shorter than 0.1 ms. For the GC_comb method, it needs to first reconstruct the permittivity distributions using both the LBP and TR algorithms and then combine these two distributions using the graph cut theory. Therefore, the reconstruction time needed for the GC_comb increases sharply to about 8 ms, which is about 80 times that cost by the single-step algorithms, say LBP and TR. Obviously, most of this time is spent on the combination step but not on the reconstruction steps by the LBP and TR algorithms. Even so, such a reconstruction time can still meet the requirement to reconstruct images at a speed faster than 100 frames/s and is enough to characterize the hydrodynamic behavior in two-phase flow systems, such as gas–solid fluidized beds [11]. For the Landweber iteration technique, although good images can be obtained, its slow reconstruction speed renders it suitable only as an off-line method.

VI. Conclusion

In this paper, beyond the idea to develop a new image reconstruction algorithm, a novel graph-cut-based strategy was proposed to combine the images reconstructed by two existing image reconstruction algorithms for ECT. As an example, the proposed strategy was implemented to combine two images reconstructed by two widely used ECT reconstruction algorithms, i.e., LBP and TR. Both numerical simulations and experiments associated with stationary objects and a gas–solid fluidized bed confirmed the effectiveness of the proposed strategy. The results demonstrate that the graph-cut-based strategy can retain the good image quality in the central region reconstructed by the TR algorithm and meanwhile eliminate the artifacts by taking advantages of the LBP algorithm in the near-wall region. In this way, the quality of ECT images obtained via a single reconstruction algorithm can be greatly improved. In addition, the typical reconstruction time cost by the proposed strategy is about 8 ms, which suggests that it can be potentially used for on-line ECT measurement.

In fact, it is hard to obtain satisfactory ECT images in all imaging regions by the use of a single reconstruction algorithm. The proposed strategy in this paper opens a promising way to combine ECT images obtained by different reconstruction algorithms that is unique in retaining the advantages of these algorithms while abandoning the drawbacks. Although only the examples of the combination of the LBP and TR algorithms were presented, the strategy can certainly be extended to the combination of other image reconstruction algorithms following a similar framework. Moreover, with the ability to remove artifacts and integrate training patterns with any dimensionality, the proposed strategy shows tremendous potential for 3-D ECT image reconstruction.

References

[1] J. Yao and M. Takei, "Application of process tomography to multiphase flow measurement in industrial and biomedical fields: A review," *IEEE Sensors J.*, vol. 17, no. 24, pp. 8196–8205, Dec. 2017.

[2] T. Dyakowski, "Process tomography applied to multi-phase flow measurement," *Meas. Sci. Technol.*, vol. 7, no. 3, pp. 343–353, 1996.

[3] R. F. Mudde, "Time-resolved X-ray tomography of a fluidized bed," *Powder Technol.*, vol. 199, no. 1, pp. 55–59, Apr. 2010.

[4] C. Boyer, A. Koudil, P. Chen, and M. P. Dudukovic, "Study of liquid spreading from a point source in a trickle bed via gamma-ray tomography and CFD simulation," *Chem. Eng. Sci.*, vol. 60, no. 22, pp. 6279–6288, Nov. 2005.

[5] L. J. Xu and L. A. Xu, "Gas/liquid two-phase flow regime identification by ultrasonic tomography," *Flow Meas. Instrum.*, vol. 8, no. 3, pp. 145–155, 1998.

[6] H. Q. Che, H. G. Wang, J. M. Ye, W. Q. Yang, and Z. P. Wu, "Application of microwave tomography to investigation the wet gas-solids flow hydrodynamic characteristics in a fluidized bed," *Chem. Eng. Sci.*, vol. 180, pp. 20–32, Apr. 2018.

[7] W. Zhang, C. Wang, W. Yang, and C.-H. Wang, "Application of electrical capacitance tomography in particulate process measurement—A review," *Adv. Powder Technol.*, vol. 25, no. 1, pp. 174–188, Jan. 2014.

[8] W. Yang, "Design of electrical capacitance tomography sensors," *Meas. Sci. Technol.*, vol. 21, no. 4, p. 042001, 2010.

[9] Q. Guo *et al.*, "Investigation of gas–solid bubbling fluidized beds using ECT with a modified Tikhonov regularization technique," *AIChE J.*, vol. 64, no. 1, pp. 29–41, Jan. 2018.

[10] Q. Guo *et al.*, "Experimental verification of solid-like and fluid-like states in the homogeneous fluidization regime of geldart a particles," *Ind. Eng. Chem. Res.*, vol. 57, no. 7, pp. 2670–2686, Feb. 2018.

[11] K. Huang *et al.*, "High-temperature electrical capacitance tomography for gas–solid fluidised beds," *Meas. Sci. Technol.*, vol. 29, no. 10, Aug. 2018, Art. no. 104002.

[12] J. C. Gamio, J. Castro, L. Rivera, J. Alamilla, F. Garcia-Nocetti, and L. Aguilar, "Visualisation of gas–oil two-phase flows in pressurised pipes using electrical capacitance tomography," *Flow Meas. Instrum.*, vol. 16, nos. 2–3, pp. 129–134, Apr./Jun. 2005.

[13] Z. Gut and P. Wolanski, "Flame imaging using 3D electrical capacitance tomography," *Combustion Sci. Technol.*, vol. 182, pp. 1580–1585, 2010.

[14] W. Q. Yang and L. Peng, "Image reconstruction algorithms for electrical capacitance tomography," *Meas. Sci. Technol.*, vol. 14, no. 1, pp. R1–R13, Dec. 2003.

[15] J. Ye, H. Wang, and W. Yang, "Image reconstruction for electrical capacitance tomography based on sparse representation," *IEEE Trans. Instrum. Meas.*, vol. 64, no. 1, pp. 89–102, Jan. 2015.

[16] J. Lei, Q. Liu, and X. Wang, "Deep learning-based inversion method for imaging problems in electrical capacitance tomography," *IEEE Trans. Instrum. Meas.*, vol. 67, no. 9, pp. 2107–2118, Sep. 2018.

[17] M. Soleimani, P. K. Yalavarthy, and H. Dehghani, "Helmholtz-type regularization method for permittivity reconstruction using experimental phantom data of electrical capacitance tomography," *IEEE Trans. Instrum. Meas.*, vol. 59, no. 1, pp. 78–83, Jan. 2010.

[18] L. Jing, S. Liu, L. Zhihong, and S. Meng, "An image reconstruction algorithm based on the extended Tikhonov regularization method for electrical capacitance tomography," *Measurement*, vol. 42, no. 3, pp. 368–376, 2009.

[19] J. Zhao, L. Xu, and Z. Cao, "Direct image reconstruction for electrical capacitance tomography using shortcut D-bar method," *IEEE Trans. Instrum. Meas.*, vol. 68, no. 2, pp. 483–492, Feb. 2018.

[20] W. Q. Yang, D. M. Spink, T. A. York, and H. McCann, "An image-reconstruction algorithm based on Landweber's iteration method for electrical-capacitance tomography," *Meas. Sci. Technol.*, vol. 10, no. 11, pp. 1065–1069, 1999.

[21] L. H. Peng, H. Merkus, and B. Scarlett, "Using regularization methods for image reconstruction of electrical capacitance tomography," *Part. Part. Syst. Characterization*, vol. 17, no. 3, pp. 96–104, Oct. 2000.

[22] C. G. Xie, A. Plaskowski, and M. S. Beck, "8-electrode capacitance system for two-component flow identification. I. Tomographic flow imaging," *IEE Proc. A, Phys. Sci., Meas. Instrum., Manage. Educ.*, vol. 136, no. 4, pp. 173–183, Jul. 1989.

[23] Q. Xue, H. Wang, Z. Cui, and C. Yang, "Electrical capacitance tomography using an accelerated proximal gradient algorithm," *Rev. Sci. Instrum.*, vol. 83, no. 4, Apr. 2012, Art. no. 043704.

[24] Y. Wang, H. Song, and Y. Zhang, "Spectral-spatial classification of hyperspectral images using joint bilateral filter and graph cut based model," *Remote Sens.*, vol. 8, no. 9, p. 748, Sep. 2016.
[25] D. Cheng, G. Meng, S. Xiang, and C. Pan, "Efficient sea–land segmentation using seeds learning and edge directed graph cut," *Neurocomputing*, vol. 207, pp. 36–47, Sep. 2016.
[26] M. Unberath, S. Achenbach, R. Fahrig, and A. Maier, "Exhaustive graph cut-based vasculature reconstruction," presented at the IEEE 13th Int. Symp. Biomed. Imag., Prague, Czech Republic, Apr. 2016, pp. 1143–1146.
[27] T. Zahner, T. Lochbühler, G. Mariethoz, and N. Linde, "Image synthesis with graph cuts: A fast model proposal mechanism in probabilistic inversion," *Geophys. J. Int.*, vol. 204, no. 2, pp. 1179–1190, Feb. 2015.
[28] X. Li, G. Mariethoz, D. Lu, and N. Linde, "Patch-based iterative conditional geostatistical simulation using graph cuts," *Water Resour. Res.*, vol. 52, no. 8, pp. 6297–6320, Aug. 2016.
[29] L. Peng, J. Ye, G. Lu, and W. Yang, "Evaluation of effect of number of electrodes in ECT sensors on image quality," *IEEE Sensors J.*, vol. 12, no. 5, pp. 1554–1565, May 2012.
[30] J. Ye, H. Wang, and W. Yang, "Evaluation of electrical capacitance tomography sensor based on the coupling of fluid field and electrostatic field," *Meas. Sci. Technol.*, vol. 27, no. 7, May 2016, Art. no. 074003.
[31] C. G. Xie *et al.*, "Electrical capacitance tomography for flow imaging: system model for development of image reconstruction algorithms and design of primary sensors," *IEE Proc. G-Circuits, Devices Syst.*, vol. 139, no. 1, pp. 89–98, Feb. 1992.
[32] D. Calvetti, S. Morigi, L. Reichel, and F. Sgallari, "Tikhonov regularization and the L-curve for large discrete ill-posed problems," *J. Comput. Appl. Math.*, vol. 123, nos. 1–2, pp. 423–446, Nov. 2000.
[33] F. S. V. Bazán, "Simple and efficient determination of the Tikhonov regularization parameter chosen by the generalized discrepancy principle for discrete ill-posed problems," *J. Sci. Comput.*, vol. 63, no. 1, pp. 163–184, Apr. 2014.
[34] V. Kwatra, A. Schödl, I. Essa, G. Turk, and A. Bobick, "Graphcut textures: Image and video synthesis using graph cuts," *ACM Trans. Graph.*, vol. 22, no. 3, pp. 277–286, Jul. 2003.
[35] Y. Boykov and G. Funka-Lea, "Graph cuts and efficient N-D image segmentation," *Int. J. Comput. Vis.*, vol. 70, no. 2, pp. 109–131, Nov. 2006.
[36] Y. Boykov and V. Kolmogorov, "An experimental comparison of min-cut/max-flow algorithms for energy minimization in vision," *IEEE Trans. Pattern Anal. Mach. Intell.*, vol. 26, no. 9, pp. 1124–1137, Sep. 2004.
[37] W. Q. Yang and T. A. York, "New AC-based capacitance tomography system," *IEE Proc.-Sci., Meas. Technol.*, vol. 146, no. 1, pp. 47–53, Jan. 1999.
[38] J. Ye, H. Wang, Y. Li, and W. Yang, "Coupling of fluid field and electrostatic field for electrical capacitance tomography," *IEEE Trans. Instrum. Meas.*, vol. 64, no. 12, pp. 3334–3353, Dec. 2015.
[39] Z.-K. Gao, P.-C. Fang, M.-S. Ding, and N.-D. Jin, "Multivariate weighted complex network analysis for characterizing nonlinear dynamic behavior in two-phase flow," *Exp. Therm. Fluid Sci.*, vol. 60, pp. 157–164, Jan. 2015.
[40] Y. Li and D. J. Holland, "Fast and robust 3D electrical capacitance tomography," *Meas. Sci. Technol.*, vol. 24, no. 10, p. 105406, 2013.
[41] R. K. Rasel, C. E. Zuccarelli, Q. M. Marashdeh, L.-S. Fan, and F. L. TeixeiraIEEE, "Toward multiphase flow decomposition based on electrical capacitance tomography sensors," *IEEE Sens. J.*, vol. 17, no. 24, pp. 8027–8036, Dec. 2017.

Qiang Guo received the B.Eng. degree from Yunnan University, Kunming, China, in 2014. He is currently pursuing the Ph.D. degree with the Dalian Institute of Chemical Physics, Chinese Academy of Sciences, Dalian, China.

His current research interests include measurement and simulation of multiphase flows.

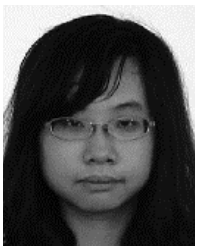

Xue Li received the B.S. and Ph.D. degrees from the University of Science and Technology of China, Hefei, China, in 2011 and 2016, respectively.

She joined the Dalian Institute of Chemical Physics, Chinese Academy of Sciences, Dalian, China, in 2016. Her current research interests include measurement and simulation of multiphase flows and engineering computation.

Baolin Hou received the B.S. degree from the Taiyuan University of Technology, Taiyuan, China, in 2006, and the Ph.D. degree from the Institute of Process Engineering, Chinese Academy of Sciences, Beijing, China, in 2011.

He joined the Dalian Institute of Chemical Physics, Chinese Academy of Sciences, Dalian, China, in 2011. His current research interests include chemical reaction engineering.

Gregoire Mariethoz received the M.S., M.A.S., and Ph.D. degrees from the University of Neuchâtel, Neuchâtel, Switzerland, in 2003, 2006, and 2009, respectively.

From 2009 to 2010, he was a Post-Doctoral Researcher with Stanford University, Stanford, CA, USA, and from 2010 to 2014, he was a Senior Lecturer with the University of New South Wales, Sydney, NSW, Australia. Since 2014, he has been a Professor with the University of Lausanne, Lausanne, Switzerland. His current research interests include the development of spatial statistics algorithms and their application in Earth surface observation, hydrology and hydrogeology.

Mao Ye received the B.Eng. degree from the Jiangsu University of Science and Technology, Zhenjiang, China, in 1994, and the M.Eng. and Ph.D. degrees from Southeast University, Nanjing, China, in 1997 and 2000, respectively.

From 2000 to 2006, he was a Research Fellow with the University of Twente, Enschede, The Netherlands, and the Eindhoven University of Technology, Eindhoven, The Netherlands, and from 2009 to 2010, he was an FCC Process Engineer with Shell Global Solutions International B.V., Amsterdam, The Netherlands. Since 2010, he has been a Professor with the Dalian Institute of Chemical Physics, Chinese Academy of Sciences, Dalian, China. He has published more than 50 papers and has filed more than 100 patents. His current research interests include multiphase catalytic processes, measurement and simulation of multiphase flows, and industrial fluidized bed reactors.

Dr. Ye was a recipient of the Outstanding Research Achievement Award from the Chinese Academy of Sciences, China, in 2011, the Newton Advanced Fellowship from the Royal Society, U.K., in 2015, and the National Ten Thousand Talent Program, China, in 2017.

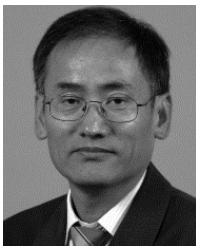

Wuqiang Yang (SM'05–F'12) received the B.Eng. (Hons.), M.S., and Ph.D. (Hons.) degrees from Tsinghua University, Beijing, China, in 1982, 1985, and 1988, respectively.

After three years as a Lecturer with Tsinghua University, he joined the University of Manchester Institute of Science and Technology (now The University of Manchester), Manchester, U.K., in 1991, where he has been a Professor since 2005. He has published more than 300 papers. His current research interests include instrumentation, measurement, and electrical capacitance tomography.

Dr. Yang received many awards for his research. He is an editorial board member/associate editor of six journals and a guest editor of nearly ten journal special issues, and he reviews papers for more than 40 journals. He also organized many conferences, in particular the IEEE International Conference on Imaging Systems and Techniques. He is an IEEE Instrumentation and Measurement Society Distinguished Lecturer from 2010 to 2016. Since 2002, his biography has been in *Who's Who in the World*.

Zhongmin Liu received the B.S. degree from Zhengzhou University, Zhengzhou, China, in 1983, and the M.S. and Ph.D. degrees from the Dalian Institute of Chemical Physics, Chinese Academy of Sciences, Dalian, China, in 1986 and 1990, respectively.

He has been a Professor and the Director of the Dalian Institute of Chemical Physics, Chinese Academy of Sciences, since 1996 and 2017, respectively. As a Leading Scientist, he successfully developed the DMTO technology and licensed the world's first industrial MTO unit. He has published more than 300 papers and has filed more than 600 patents. His current research interests include methanol to olefins (MTO), coal chemistry, and zeolite catalysis.

Dr. Liu is a member of the International Academic Committee of the 13th, 14th, and 17th International Zeolite Conference. He was elected as the member of the Chinese Academy of Engineering in 2015. He has received many awards, including the First Prize of the National Technological Invention Awards, China, in 2014, and the HLHL Science and Technology Innovation Award in 2015.